A Parameter-Independent Optimal Field-Weakening Control Strategy of IPMSM for Electric Vehicles Over Full Speed Range

Zhuoran Huang, Cheng Lin, and Jilei Xing

***Abstract*—The rest if this article proposes a field-weakening control strategy along with two characteristic curves of IPMSM under electric vehicle driving conditions, where the operation speed, load torque, and target torque change rapidly and continuously. Two characteristic curves, the maximum torque curve, and the switching torque curve are introduced to obtain a strategy that can generate the optimal operation point with minimum stator current at any machine speed. The reference current of the optimal operation points can be derived from both calculation method and conventional calibration method. However, sometimes it is difficult to get solutions directly by the calculation method, not to mention it relies on precise motor parameters that vary with the temperature and magnetic saturation. Additionally, conventional calibration method is really a time-consuming process. In this article, a much simpler approach to obtain reference current based on polynomial fitting is presented, which has a great performance on fitting precision and much less workload with only one additional operation point to be calibrated except for the two characteristic curves. With this fitting method, the reference current generation procedure becomes completely parameter independent. The proposed strategy is demonstrated through simulations and test bench results.**

***Index Terms*—Electric vehicles (EVs), field weakening (FW), interior permanent magnet synchronous motor (IPMSM), optimal control, parameter independent[1].**

NOMENCLATURE

α - β	Stationary axis reference frame quantities.
d - q	Synchronous axis reference frame quantities.
u, i	Stator voltage and current.
$U_{\rm lim}$, $I_{\rm lim}$	Maximum amplitude of stator voltage and current.
R, L	Resistance and inductance of stator winding.
λ_{dq}, ψ_{dq}	Stator flux and PM flux.
$n_{\rm p}$	Number of pole pairs.
$\omega_{\rm r}$	Electrical speed.
T_e	Expected output torque.
$T_{\rm max}$, T_p	Maximum torque and switching torque.
η	Accelerator pedal position.
C_i	Coefficient of unary polynomial.
p	Differential operator.
T	Ambient temperature.

Manuscript received September 4, 2019; revised February 1, 2020, May 14, 2020, and July 31, 2020; accepted September 8, 2020. Date of publication September 18, 2020; date of current version November 20, 2020. This work was supported in part by the National Key Research and Development Program of China under Grant 2017YFB0103801 and in part by the National Natural Science Foundation of China under Grant 51975049. Recommended for publication by Associate Editor K. Akatsu. *(Corresponding author: Zhuoran Huang.)*

The authors are with the School of Mechanical Engineering, Beijing Institute of Technology, Beijing 100081, China (e-mail: huangzhuoran1994@163.com; lincheng@bit.edu.cn; xingjilei699@163.com).

Color versions of one or more of the figures in this article are available online at https://ieeexplore.ieee.org.

Digital Object Identifier 10.1109/TPEL.2020.3024701

[1]Parameter independent, in this article, indicates that the machine parameters need not be obtained in advance.

I. INTRODUCTION

THE development of electric vehicles (EVs) is highlighted in recent years with the energy crisis getting severer. Among all potential options for traction motors of EVs, interior permanent magnet synchronous motors (IPMSMs) are adopted extensively due to its positive features such as low volume, high power density, high efficiency, and wide speed range [1]. However, IPMSM control is not so easy as that of previous dc drives [2]. For these reasons, plenty of control methods have been proposed to achieve better performance of IPMSM drives under modern applications. Two most notable control methods are direct torque control (DTC) and field weakening (FW) control, which is also called vector control (VC) [3]–[5].

A conventional FW control strategy for IPMSM is to maintain the direct axis (d-axis) component of the stator current at zero [6] so that the entire current vector is aligned along the quadrature axis (q-axis), which makes the output torque proportional to the q-axis component of the stator current. Though the control will become easier with zero d-axis current, the steady-state performance of IPMSM in high speed range is severely degraded because the reluctance torque cannot be utilized [7]. Moreover, the operation speed of IPMSM will be also limited to a rated value with the constraints of current and voltage [8]. In order to obtain the maximum efficiency and extend the speed range of IPMSM, many field-weakening control strategies have been proposed based on the multiple optimal trajectories and boundaries, including the maximum torque per ampere (MTPA) trajectory, the current limit circle, and the maximum torque per voltage (MTPV) trajectory. A typical strategy is generating current vectors that track along the MTPA trajectory [9]. Furthermore, all these field-weakening control strategies can be classified into feedforward and feedback methods [8]. Feedforward methods [10], [11] adopt reference currents that are determined experimentally or analytically. Feedback methods [12], [13] use a feedback from the terminal voltage to track

the voltage limitation. The feedback metrics can be various, including the voltage error, output speed error, or even *q-axis* current error [14]. Combined with some other control techniques, e.g., fuzzy control [15], adaptive robust control [16], model predictive control (MPC) [17], and sliding mode control [18], these conventional field-weakening control strategies have shown proper control performance and dynamic response for IPMSMs by arranging the operation point along the optimal trajectory.

However, in most cases, the target of all aforementioned field-weakening control strategies is to obtain the most rapid and accurate speed response, which is suitable for some servo applications such as air/oil pumps and machine tools instead of traction systems of EVs. Usually, for an EV, the instructions are given by the driver through the accelerator pedal and processed into torque values by the vehicle control unit (VCU), resulting in high requirements for rapid dynamic torque response characteristics of the control strategies [19]. A common way of torque control for the IPMSM in literatures is DTC, which is also employed for speed control in many areas. Compared with FW control, DTC does not need the motor model except for the stator resistance, making itself insensitive to parameter variation [20]. However, DTC has to suffer from some serious drawbacks including high torque and flux ripples, and variable switching frequency [21]. Inoue *et al.* [22] compared the FW and DTC performance in different cases.

In fact, most control strategies for EV traction motors are put forward based on FW methods. Compared with feedforward FW methods, feedback methods have an extra outer loop (typically a voltage loop) that needs decoupling in dynamics [23], which may affect dynamic behavior of EVs, i.e., have a worse transient response. Therefore, feedforward methods are more fitting for EV driving conditions. However, the motor model should be reasonably well known to provide precise motor parameters [8]. Besides, obtaining reference currents with feedforward methods require solving fourth-order equations online, with motor parameters varying with temperature and magnetic saturation. Alternatively, look-up tables for reference currents [24], [25], which can be obtained by calibration, are extensively applied in torque control in the field of EVs. However, conventional calibration requires a huge amount of operation points to improve the control precision.

This article proposes an optimal FW control approach, which can be categorized as a feedforward-based current VC method. An optimal operation point selection algorithm is designed, where all the operation points are classified into two types: Type I and Type II. The reference currents of Type I points can be obtained directly from the calibration results where only two characteristic curves need to be calibrated. For Type II points, an equation based on polynomial fitting is given to calculate the reference currents. The innovation of this approach is that it combines the advantages of both calculation and calibration methods. Conventional calculation method can compute more precise current references but requires obtaining intersections between the voltage limit ellipse and torque hyperbola. Conventional calibration method is parameter independent but really takes too much time even when not accounting for temperature or dc-link voltage variations. The approach in this article is both parameter independent and time-saving, meanwhile has no need of solving complex equations online or calibrating all the reference vectors.

The rest of this article is organized as follows. The fundamental electromagnetic model of IPMSM and the description of MTPA and MTPV are described in Section II. In Sections III and IV, the novel characteristic curves and field-weakening control strategy are introduced and analyzed. In Section V, the parameter independent control method is designed to avoid solving fourth-order equations. In Section VI, local optimization is implemented to improve the model consistency based on known operation points. The performances of the proposed strategy are verified by simulations and experimental results in Section VII. Additionally, it should be addressed that, in Section VII, the experimental results are obtained based on (23), considering the temperature effects and parameter variations. Finally, Section VIII concludes the article.

II. PMSM Model and Operation Constraints

The mathematical model of a PMSM defined in the rotating reference frame *d-q* [26] can be expressed by

$$u_{\mathrm{s}} = R_{\mathrm{s}} i_{\mathrm{s}} + \omega_{\mathrm{r}} J \psi_{\mathrm{s}} + p\psi_{\mathrm{s}} \tag{1}$$

$$T_{\mathrm{e}} = \frac{3}{2} n_{\mathrm{p}} i_{\mathrm{q}} (\psi_{\mathrm{f}} - \beta L_{\mathrm{d}} i_{\mathrm{d}}) \tag{2}$$

where

$$u_{\mathrm{s}} = [u_{\mathrm{d}}, u_{\mathrm{q}}]^{\mathrm{T}}$$

$$i_{\mathrm{s}} = [i_{\mathrm{d}}, i_{\mathrm{q}}]^{\mathrm{T}}$$

$$R_{\mathrm{s}} = \begin{bmatrix} R & 0 \\ 0 & R \end{bmatrix}$$

$$J = \begin{bmatrix} 0 & -1 \\ 1 & 0 \end{bmatrix}$$

$$\lambda_{dq} = [L_{\mathrm{d}} i_{\mathrm{d}} + \psi, L_{\mathrm{q}} i_{\mathrm{q}}]^{\mathrm{T}}$$

$$\beta = \rho - 1$$

$$\rho = L_{\mathrm{q}} / L_{\mathrm{d}}.$$

u_{d}, u_{q}, i_{d}, i_{q}, L_{d}, and L_{q} are, respectively, the stator voltage components, stator current components and inductances along *d*- and *q*-axis. *R* is the phase winding resistance, ω_{r} is the electrical speed of the motor, ψ is the permanent magnet flux linkage, T_{e} is the motor torque, n_{p} is the number of pole pairs, and *p* is the differential operator.

Equation (1) can be simplified as (3) under steady state with the derivative term and the voltage drop due to the winding resistance being neglected

$$u_{\mathrm{s}} = \omega_{\mathrm{r}} J \psi_{\mathrm{s}}. \tag{3}$$

Due to the physical current and voltage constraints, there are maxima for the amplitude of stator voltage vector and stator current vector, which can be written as

$$\sqrt{{u_{\mathrm{d}}}^2 + {u_{\mathrm{q}}}^2} \le U_{\lim} \tag{4}$$

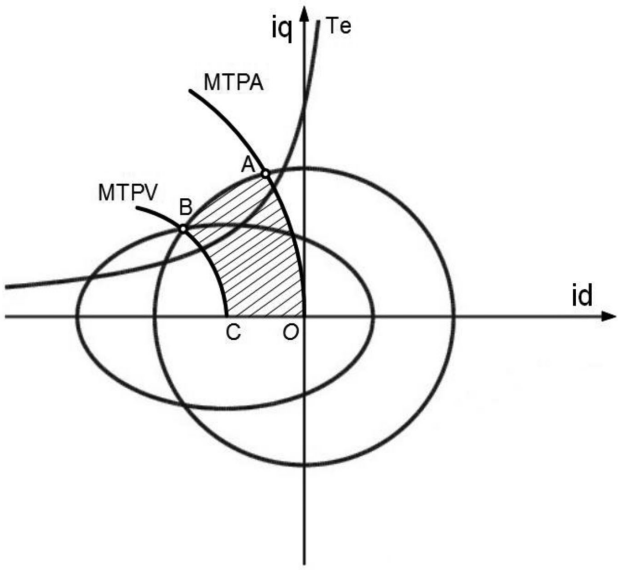

Fig. 1. Distribution area of optimal current operation points for IPMSM, bounded by MPTA trajectory, MTPV trajectory, and the current limit circle.

$$\sqrt{{i_\mathrm{d}}^2 + {i_\mathrm{q}}^2} \le I_\mathrm{lim}. \tag{5}$$

Equation (5) is known as the current limit circle in *d-q* reference frame. Substituting (3) into (4), the voltage constraints can be derived as (6), known as the voltage limit ellipses

$$\frac{(i_\mathrm{d} + \psi_\mathrm{f}/L_\mathrm{d})^2}{\rho^2} + {i_\mathrm{q}}^2 \le \left(\frac{U_\mathrm{lim}}{\omega_\mathrm{r} L_\mathrm{q}}\right)^2. \tag{6}$$

For every demanded motor torque, there exists an optimal operation point that minimizes the stator current and thus maximizes the torque per ampere. From (2) and (5), the expression of MTPA trajectory can be derived as (7) using the Lagrange multiplier method

$$i_\mathrm{q} = \sqrt{\frac{\psi_\mathrm{f} i_\mathrm{d}}{L_\mathrm{d} - L_\mathrm{q}} + {i_\mathrm{d}}^2}. \tag{7}$$

Analogously, for every demanded motor torque and operation speed, the expression of MTPV trajectory can be derived as

$$\beta {L_\mathrm{d}}^2(\rho^2 {i_\mathrm{q}}^2 - {i_\mathrm{d}}^2) + L_\mathrm{d}\psi_\mathrm{f}(1-\beta) i_\mathrm{d} + {\psi_\mathrm{f}}^2 = 0. \tag{8}$$

Actually, the MTPV trajectory is the set of *point of contact* between every voltage limit ellipse and its tangent constant torque curve. Under high-speed operation states, voltage constraints are sometimes in preference to current constraints, and the torque corresponding to the operation point on the MTPV trajectory will be the maximum motor torque at the operation speed.

Fig. 1 shows the trajectories of (2), (5), (6), (7), (8), which are the constant torque curve ($T_\mathrm{e} > 0$), current limit circle, voltage limit ellipse, MTPA trajectory, and MTPV trajectory. Based on the constraints of all aforementioned trajectories, the *optimal operation point* is defined as the point where the stator current is minimum (considering copper loss greater compared to other losses). Moreover, the *d*- and *q*-axis currents corresponding to the optimal operation point are defined to be *reference currents*. With operation speed and target torque changing continuously, the optimal operation points will be distributed within the shadow area shown in Fig. 1.

III. Optimal Operation Strategy

The driver gets the expected output torque by changing the accelerator pedal position while driving. Since the certain state and input constraints are applied to the PMSM, the maximum available torque T_max at every moment is limited as well, which can be obtained by offline calculation or test bench calibration. The approach to obtain T_max will be discussed minutely in Section IV. In fact, when the rated voltage is constant, T_max can be expressed as a piecewise function of operation speed *n*. In other words, the expected output torque T_e that driver desires at moment *t* depends on T_max and the accelerator pedal position $\eta \in [0, 1]$

$$T_e = \eta \cdot T_\mathrm{max}. \tag{9}$$

To identify the optimal operation points clearly, the analysis will be launched in *d-q* reference frame through several characteristic trajectories including the MTPA trajectory, current limit circle, voltage limit ellipse, and constant torque curve ($T_e > 0$). Considering that the torque increases along the ellipse starting at the *d*-axis, it reaches its peak at the point of contact between the ellipse and the constant torque curve that is tangential to the ellipse. Actually, this peak torque is the aforementioned *maximum torque* T_max. Then, to distinguish different operation modes, *switching point* is introduced, which is the intersection of the MTPA trajectory and the voltage limit ellipse, if it exists. Moreover, the torque corresponding to the switching point is defined to be *switching torque*. Assuming that the intersection of the MTPA trajectory and the constant torque curveT_e is classified as *Type I*, in addition, the intersection (the one closer to the *q*-axis in particular) of the voltage limit ellipse and the constant torque curve T_e is classified as *Type II*, the optimal operation point selecting strategy can be concluded as follows.

1) *Case 1:* If the switching point (Point P in Fig. 2) is located outside the current limit circle (including the condition where Point P coincides with Point A), the optimal operation point is the Type I, as shown in Fig. 2.
2) *Case 2:* If and only if there is *one* switching point (Point P in Fig. 3) located inside the current limit circle:
   a) if $T_e \le T_P$, the optimal operation point is the Type I as the red curve shown in Fig. 3;
   b) if $T_P < T_e \le T_\mathrm{max}$, the optimal operation point is the Type II as the blue curve shown in Fig. 3.
3) *Case 3:* If there are *two* switching points (Point P_1 and P_2 in Fig. 4) located inside the current limit circle:
   a) if $T_{P2} \le T_e \le T_{P1}$, the optimal operation point is the Type I as the red curve shown in Fig. 4:
   b) if $T_e < T_{P2}$ or $T_{P1} < T_e \le T_\mathrm{max}$, the optimal operation point is the Type II as the blue curve shown in Fig. 4.
4) *Case 4:* If there is only *one* switching point, which is just right the point of contact between the ellipse and the MTPA

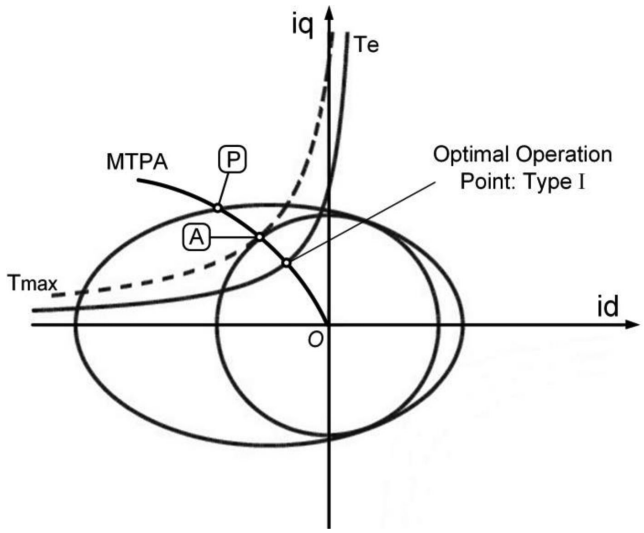

Fig. 2. Optimal operation analysis–Case 1, where the switching point is located outside the current limit circle (Point P might coincide with Point A).

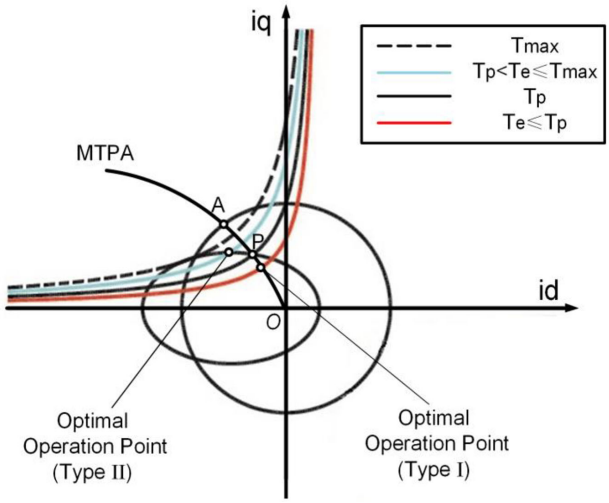

Fig. 3. Optimal operation analysis–Case 2, where the only switching point is located inside the current limit circle.

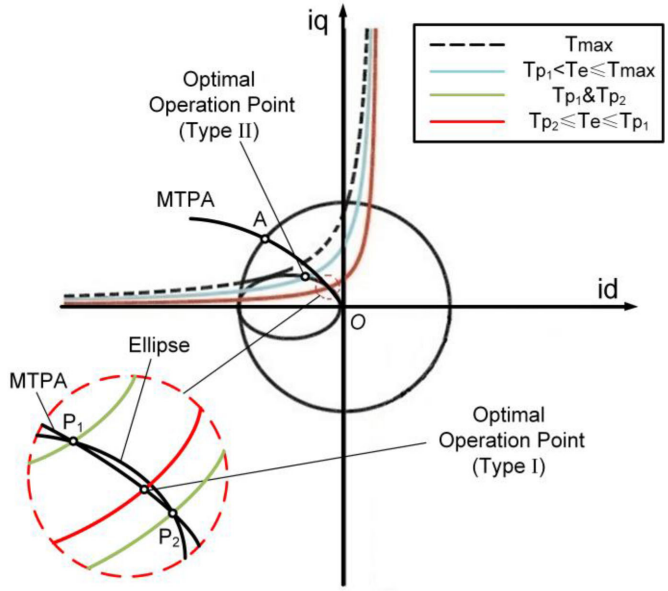

Fig. 4. Optimal operation analysis–Case 3, where there are two switching points located inside the current limit circle.

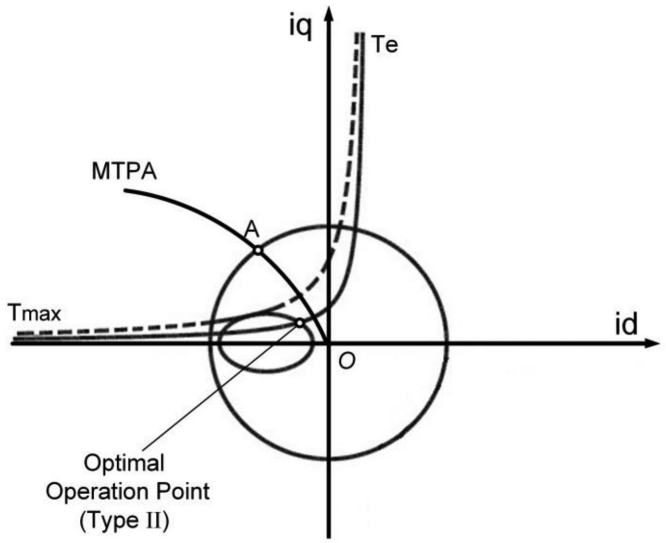

Fig. 5. Optimal operation analysis–Case 4, where there is only one switching point (point of contact between the ellipse and the MTPA trajectory) or no switching point.

trajectory, or there is no switching point at all, the optimal operation point is the Type II, as shown in Fig. 5.

Therefore, given the operation speed n and a desired torque T_e, the strategy above can generate an optimal operation point, which minimizes the current magnitude and fully utilizes the input voltage. However, the strategy has four cases with certain constraints, which are too complex for microprocessors to determine the exact location and number of switching points. To simplify and unify the four cases, the following steps are taken for the strategy.

a) In Case 1, the switching torque T_P cannot be achieved because of the current limit (with exception when Point P coincides with Point A). Considering there is no possibility of $T_P < T_{\max}$, Case 1 can be expressed in another way as follows.

Case 1:

If $T_e \leq T_P$, the optimal operation point is the Type I.

b) In Case 3, $T_e < T_{P2}$ means the velocity of the vehicle is very high and the desired torque is very small. In fact, this operation mode rarely happens for EVs during practical driving. Meanwhile, $T_e < T_{P2}$ in Case 3 corresponds to a very narrow velocity interval. Accordingly, the two operation modes in Case 3, $T_e < T_{P2}$ and $T_{P2} \leq T_e \leq T_{P1}$, are combined and regarded as one mode:

Case 3:

1) if $T_e \leq T_{P1}$, the optimal operation point is the Type I;
2) if $T_{P1} < T_e \leq T_{\max}$, the optimal operation point is the Type II.

c) In Case 4, no switching point indicates $T_P = 0$ (with exception when the MTPA trajectory is tangential to the ellipse). Thus, Case 4 can be expressed as follows.

Case 4:

If $T_P \leq T_e \leq T_{\max}$, the optimal operation point is the Type II. It is noteworthy that only when the MTPA trajectory is tangential to the ellipse ($T_P \neq 0$), there is possibility of $T_e = T_P$.

In summary, the four cases of the strategy can be unified into one standard form, which takes no account of the switching points' location and number. Supposing $T_{P1} = T_P$ in Case 3, the optimal operation point generation strategy can be concluded as follows.

After obtaining T_e and T_P:

1) if $T_e \leq T_P$, the optimal operation point is Type I:
2) if $T_P < T_e \leq T_{\max}$, the optimal operation point is Type II.

IV. Optimal Operation Analysis

The strategy obtained in Section III can cover full speed range, which means the strategy can generate the optimal operation point at any machine speed if given a desired torque and corresponding switching torque. Prior to solving for the optimal operation, the maximum torque $T_{\max}$ and the switching torque T_P must be computed or calibrated on a test bench. Instead of online calculation, offline calculation is mostly adopted due to the great amount of complicated computation that is NP hard sometimes [27]. In fact, no matter what the method is (calculation/calibration), the aim is to obtain the relationship between the operation speed, desired torque, and reference current. The difference between the two methods is: the calculation method relies on motor parameters, but the calibration method is parameter independent. In this section, only the calculation method, where $T_{\max}$ and T_P are obtained, is analyzed.

A. Maximum Torque

Limited by the current and voltage constraints, the desired torque cannot exceed the maximum torque at any operation speed. From Fig. 1, it is known that the optimal operation area is bounded by the MTPA trajectory, current limit circle, and MTPV trajectory. Consequently, the maximum torque is produced by the operation points that lie on the boundary of the area. In fact, the maximum torque varies with the operation speed and dc-link voltage. Supposing$n_A$and n_B correspond to the operation speed of Point A (intersection of the MTPA trajectory and the current limit circle) and Point B (intersection of the MTPV trajectory and the current limit circle), respectively, in Fig. 1, the maximum torque can be divided into three modes by the operation speed *n* as follows.

1) $n \leq n_A$: Here, the maximum torque is produced by Point A, which lies on the MTPA trajectory and reaches the current limit, which is always located inside the ellipse. In this condition, the PMSM is said to work in *constant torque mode* and n_A is named *rated operation speed* [8], [28], [29].
2) $n_A < n \leq n_B$: Here, T_A which is the torque corresponding to Point A cannot be achieved due to the voltage limit. Instead, the maximum torque is produced by the intersection of the current limit circle and the voltage limit ellipse, where both the stator current and voltage magnitude reach the peak and keep constant. Consequently, the PMSM is said to work in a *constant power mode* [8], [30].
3) $n > n_B$: Here, the maximum torque is produced by the intersection of the MTPV trajectory and the voltage limit ellipse, where the voltage is nominal but the current magnitude is reduced as the operation speed increases. In this condition, the PMSM is said to work in a *decreased power mode* [8], [28], [30].

Accordingly, the maximum torque characteristic corresponds to locus Point *A-AB-BC* in Fig. 1. Moreover, the characteristic of $T_{\max}$ can be written as

$$T_{\max} = \begin{cases} T_A & n \leq n_A \\ T_{AB}(n) & n_A < n \leq n_B \\ T_{BC}(n) & n > n_B. \end{cases} \tag{10}$$

The detailed equations, which are difficult for online computation, are given in the Appendix.

B. Switching Torque

After obtaining T_e from (9), the type of optimal operation point can be determined by comparing T_e with T_P. Similarly, the switching torque T_P can be also expressed as a piecewise function of operation speed *n*.

1) In constant torque mode ($n \leq n_A$), the PMSM can be operated exclusively on the MTPA trajectory, which indicates that the optimal operation point must be Type I. Considering the strategy aforementioned in Section III, let $T_P = T_{\max} = T_A$.
2) In constant power mode and decreased power mode ($n > n_A$), the switching torque is generated by the intersection of the MTPA trajectory and the voltage limit ellipse. From (6) and (7), *d*-axis current of the switching point can be computed as

$$i_{d,T_p} = \frac{-B - \sqrt{B^2 - 4A\left(\psi_f^2 - \frac{U_{\lim}^2}{\omega_r^2}\right)}}{2A} \tag{11}$$

where

$$A = L_d^2 + L_q^2$$

$$B = \frac{\psi_f L_q^2}{L_d - L_q} + 2\psi_f L_d.$$

Obviously, when $B^2 - 4A(\psi_f^2 - U_{\lim}^2/\omega_r^2) < 0$, there is no intersection between the MTPA trajectory and voltage limit ellipse, which indicates that it is impossible for the PMSM to operate on the MTPA trajectory and, meanwhile, the optimal operation point must be Type II. Letting $T_P = 0$ under this case would satisfy the strategy presented in Section III. However, no intersection ($T_P = 0$) means the whole ellipse falls in the left half of the *d-q* reference frame, which leads to $\omega_r > U_{\lim}/\psi_f$ according to (6). For EVs' PMSMs, $\omega_r > U_{\lim}/\psi_f$ is usually too high to reach in practice because of some restrictions such as the mechanical stress limits of the output shaft. Hence, $T_P = 0$

is ignored in this article. Then, the expression of T_P against n ($n > n_A$) can be obtained by substituting (11) into (2)

$$T_P = \frac{3}{2} n_{\mathrm{p}} i_{q,T_p} (\psi_{\mathrm{f}} - \beta L_{\mathrm{d}} i_{d,T_p}) \tag{12}$$

where i_{q,T_p} can be obtained by substituting (11) into (7). Obviously, the detailed equation of (12) is too complicated for real-time calculation. Nevertheless, the calculation can be done during the system initialization and then saved in RAM.

As a result, the equation of T_P can be summarized as

$$T_P = \begin{cases} T_{\max} & n \le n_A \\ 1.5 n_{\mathrm{p}} i_{q,T_p} (\psi_{\mathrm{f}} - \beta L_{\mathrm{d}} i_{d,T_p}) & n > n_A. \end{cases} \tag{13}$$

V. Parameter Independent Control Method

When the optimal operation point is Type I, it is not complicated to calculate the reference current by substituting (7) into (2). However, when it comes to Type II, the computational complexity of solving simultaneous (2) and (6) requires a huge amount of microprocessor resources for running it. Meanwhile, generally speaking, the precision of motor parameters cannot meet the high demands of applications in EV driving. Furthermore, motor parameters would vary with operation temperature and magnetic saturation in reality. All of the above make it necessary to implement calibration method, which is parameter independent.

Both the maximum torque curve and the MTPA trajectory can be obtained by calibration on a test bench. From Section III, it is known that the switching point and Type I operation point lie on the MTPA trajectory, which indicates that the reference current of Type I point can be derived directly from the calibration results. However, it would take rather a long time to obtain enough Type II operation points for precise torque control on a test bench. Based on the analysis in Sections III and IV, there exists a positive correlation between the amplitude of i_d and T_e at a certain speed, which is approximately linear, as can be shown in Fig. 6 (motor parameters needed in simulations are given in Section VII). Therefore, a relatively simple approach to obtain the reference current of Type II operation point and meanwhile reduce the calibration time is acquired by adopting linear fitting method with the switching torque curve and the maximum torque curve, both of which should be acquired in advance to determine the operation point type. The fitting equation can be written as

$$i_d = \frac{T_e - T_p}{T_{\max} - T_p} (i_{d,T\max} - i_{d,Tp}) + i_{d,Tp} \tag{14}$$

then the reference value of i_{q} can be derived according to (6). By this means, only the switching torque curve and the maximum torque curve need to be calibrated, resulting in about half cut of the calibration time as well as the data size of lookup tables for motor traction. Even though the linear fitting method is perfectly suitable for digital-signal-processor (DSP) based control, the fitting error may exceed the allowed value range for motor traction in EVs, which leads to a torque error within 6%, as can be shown in Fig. 7.

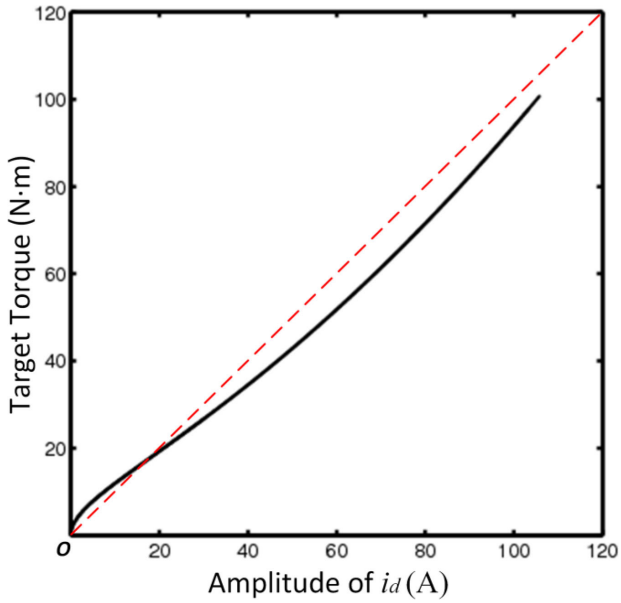

Fig. 6. Positive correlation between the amplitude of i_d and target torque.

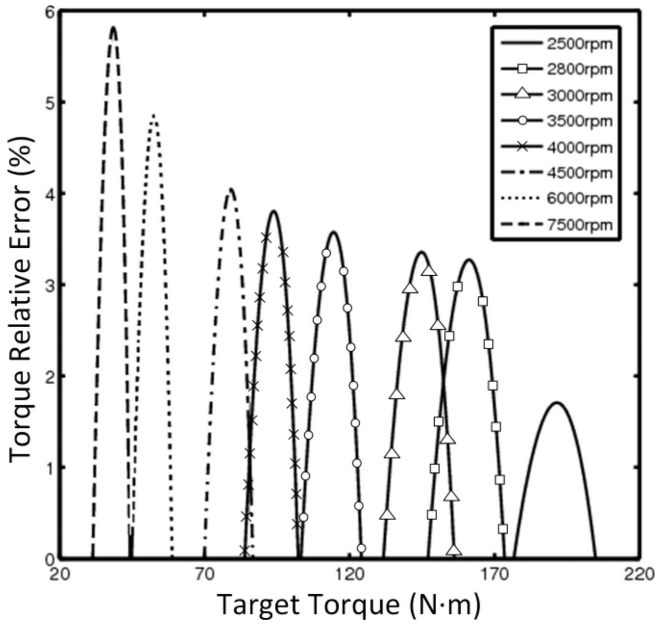

Fig. 7. Output torque relative errors under different machine speeds using the linear fitting method.

An orthodox method to reduce the fitting error is polynomial fitting, considering the nonlinear relationship between the amplitude of i_d and T_e. A unary polynomial is used here

$$i_d(\triangle T) = \sum_{i=1}^{n} C_i \triangle T^i + i_{d,Tp} \tag{15}$$

where $\triangle T = T_e - T_p$, and C_i is the coefficient of the polynomial. For a certain operation speed, $i - 1$additional operation points need to be calibrated using this fitting method, resulting in

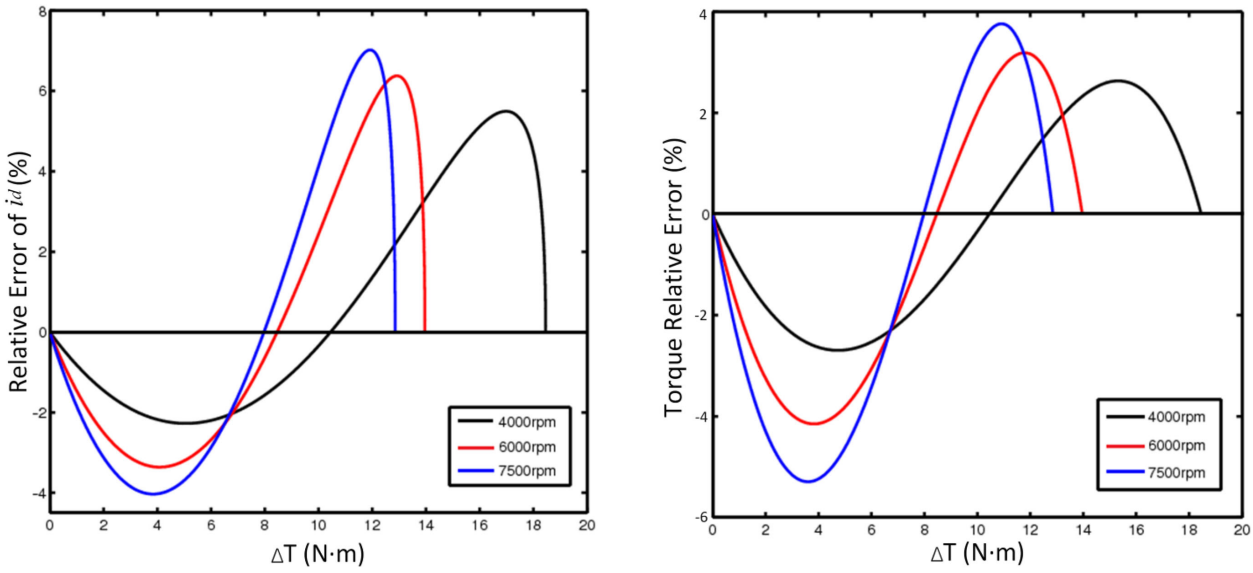

(a) (b)

Fig. 8. Simulation results of the fitting error when using quadratic polynomial fitting. (a) Relative error of i_d against $\triangle T$. (b) Relative error of the output torque against $\triangle T$.

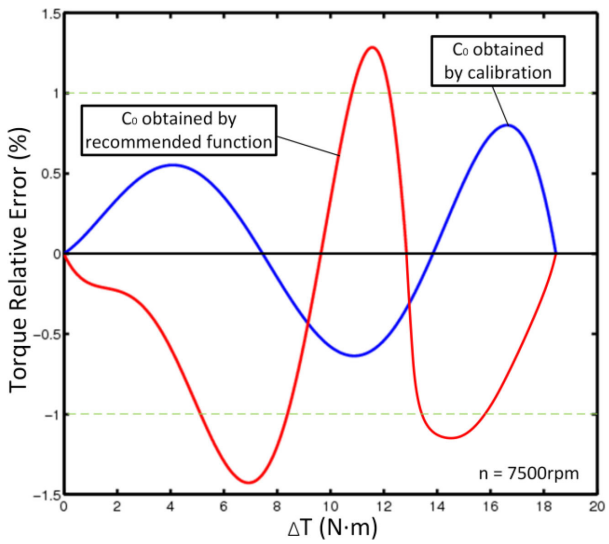

Fig. 9. Fitting error comparison between two methods that use different ways to obtain C_0.

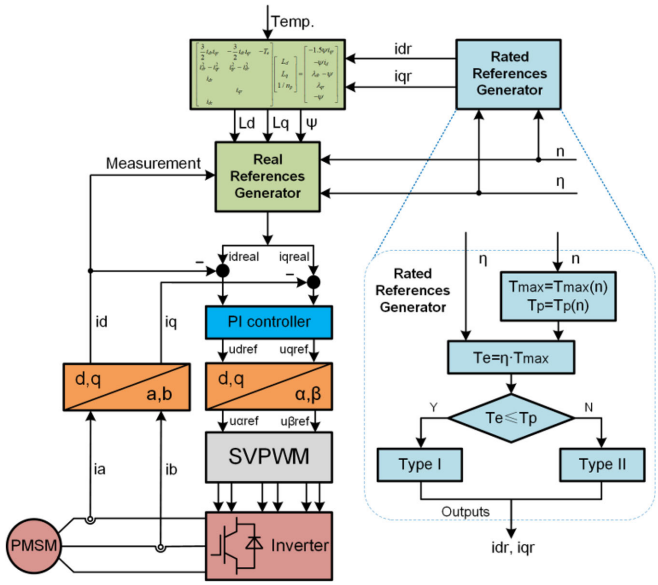

Fig. 10. Optimal operation generation procedure. The real references generator has the same configuration with the rated generator. The difference is the model inside the real references generator uses the parameters obtained by the local optimization, which considers the parameter variations.

almost the same calibration time as the conventional calibration method.

A balance between the fitting precision and calibration workload can be reached by studying the algebraic relation between i_d and T_e [31], [32]. As previously mentioned in Sections III and IV, only Type II operation points need to be computed by fitting method, which must be on the voltage limit ellipse. Considering (2) and (6), the algebraic relation between i_d and T_e is derived as

$$\frac{(i_{\mathrm{d}}+\psi_{\mathrm{f}}/L_{\mathrm{d}})^2}{\rho^2}+\frac{4{T_e}^2}{9{n_p}^2(\psi_{\mathrm{f}}-\beta L_d i_d)^2}=\left(\frac{U_{\lim}}{\omega_{\mathrm{r}}L_{\mathrm{q}}}\right)^2. \quad (16)$$

Even though it will be rather hard to solve a complex fourth-order equation like (16), the relation between i_d and T_e can be rewritten as

$$i_d(\triangle T)=C_{1/2}\triangle T^{\frac{1}{2}}+C_1\triangle T+C_{3/2}\triangle T^{\frac{3}{2}}+C_2\triangle T^2 + i_{d,Tp}. \quad (17)$$

TABLE I
MAIN PARAMETERS OF IPMSM

Parameter	Rated Value
Pole pairs	4
Stator resistance	0.004 Ω
Inductance (d-axis)	0.94 mH
Inductance (q-axis)	1.5 mH
PM rotor flux	0.055 Wb
Shaft friction	0.008 N·m·s
Shaft inertia	0.96 kg·m^2
DC-link voltage	580 V

As the operation point for $T_{\max}$ is known, it is enough to resolve all the coefficients in (17) with three additional operation points calibrated. It should be stressed here that the fitting precision will not be ruined as a result of saturation and cross saturation because all the coefficients are calibrated with the parameter variations included. However, there is still an inevitable problem preventing this method being well used in practice, which is the computational complexity. Too much root operation will be a great burden for the digital-signal processor, which has a bad influence on the time sequence regularity of control system.

Substituting an unknown function for the terms with radical exponent in (17), the equation is as follows:

$$i_d(\triangle T) = f(\triangle T) + C_1 \triangle T + C_2 \triangle T^2 + i_{d,Tp}. \quad (18)$$

With the unknown function omitted temporarily and the operation point for $(T_{\max} + T_p)/2$ gotten on the test bench, C_1 and C_2 can be resolved easily. The fitting error of i_d and output torque with this method is given in Fig. 8(a) and (b), respectively, which is approximately a sinusoid. Even though the motor parameters can be different, the relative direction between the constant torque curve and its center of curvature is fixed, which means the tendency of fitting error would not change. Based upon the above mentioned, it is reasonable to believe that the fitting error can be reduced by regarding $f(\triangle T)$ as a sine function in (18), and the fitting equation is as follows:

$$i_d(\triangle T) = C_0 \sin(\omega \triangle T) + C_1 \triangle T + C_2 \triangle T^2 + i_{d,Tp} \quad (19)$$

where

$$\omega = \frac{2\pi}{T_{\max} - T_p} \quad (20)$$

and C_0 can be resolved with an additional operation point being calibrated. The relative error of output torque with this method is reduced to less than 1%, which can be shown as the blue curve in Fig. 10.

Furthermore, to simplify the calibration process, C_0 can be set as a function of C_1 and C_2 based on the experimental data.

A recommended function is

$$C_0 = k\left[C_1 \frac{T_{\max} - T_p}{2} + C_2 \frac{(T_{\max} - T_p)^2}{4}\right] \quad (21)$$

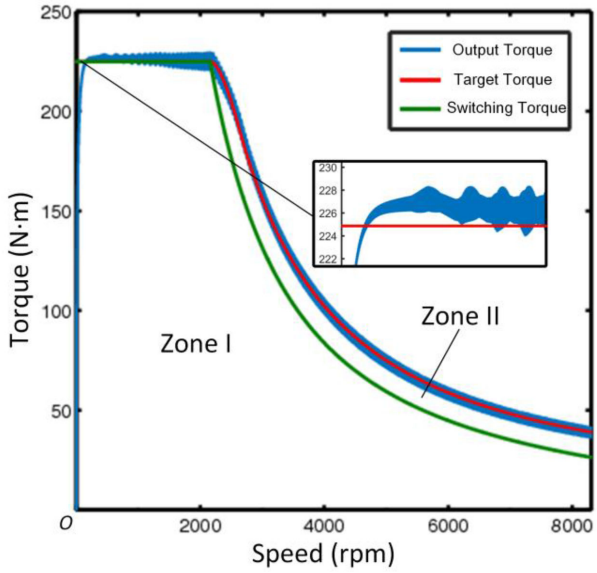

Fig. 11. Simulation results of torque versus speed with $\eta = 1$ under the ideal condition.

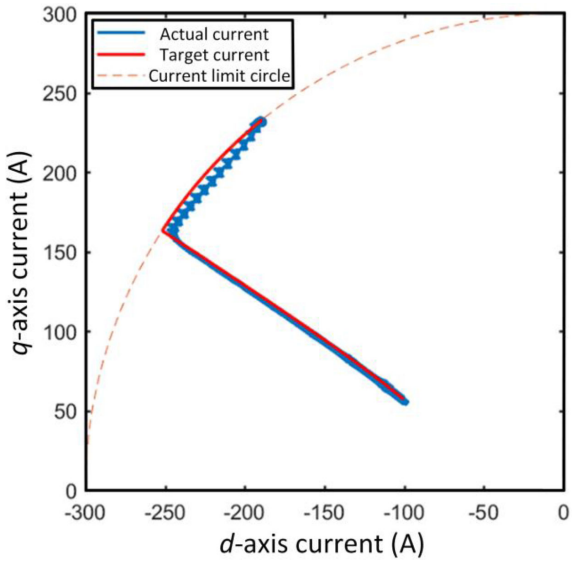

Fig. 12. Simulation results of the operation point distribution with $\eta = 1$ under the ideal condition.

where k has a value between 0.1 and 0.3. The relative error of output torque when supposing k as 0.15 is shown as the red curve in Fig. 9, which is no more than 1.5%. As all mentioned above, the final fitting method has a great and significant performance on fitting precision and much less calibration workload with only one additional operation point to be calibrated except for the switching torque curve and the maximum torque curve.

VI. LOCAL OPTIMIZATION CONSIDERING PARAMETER VARIATIONS

The proposed strategy relies on a sufficiently accurate PMSM model and its main characteristic curves (the maximum torque

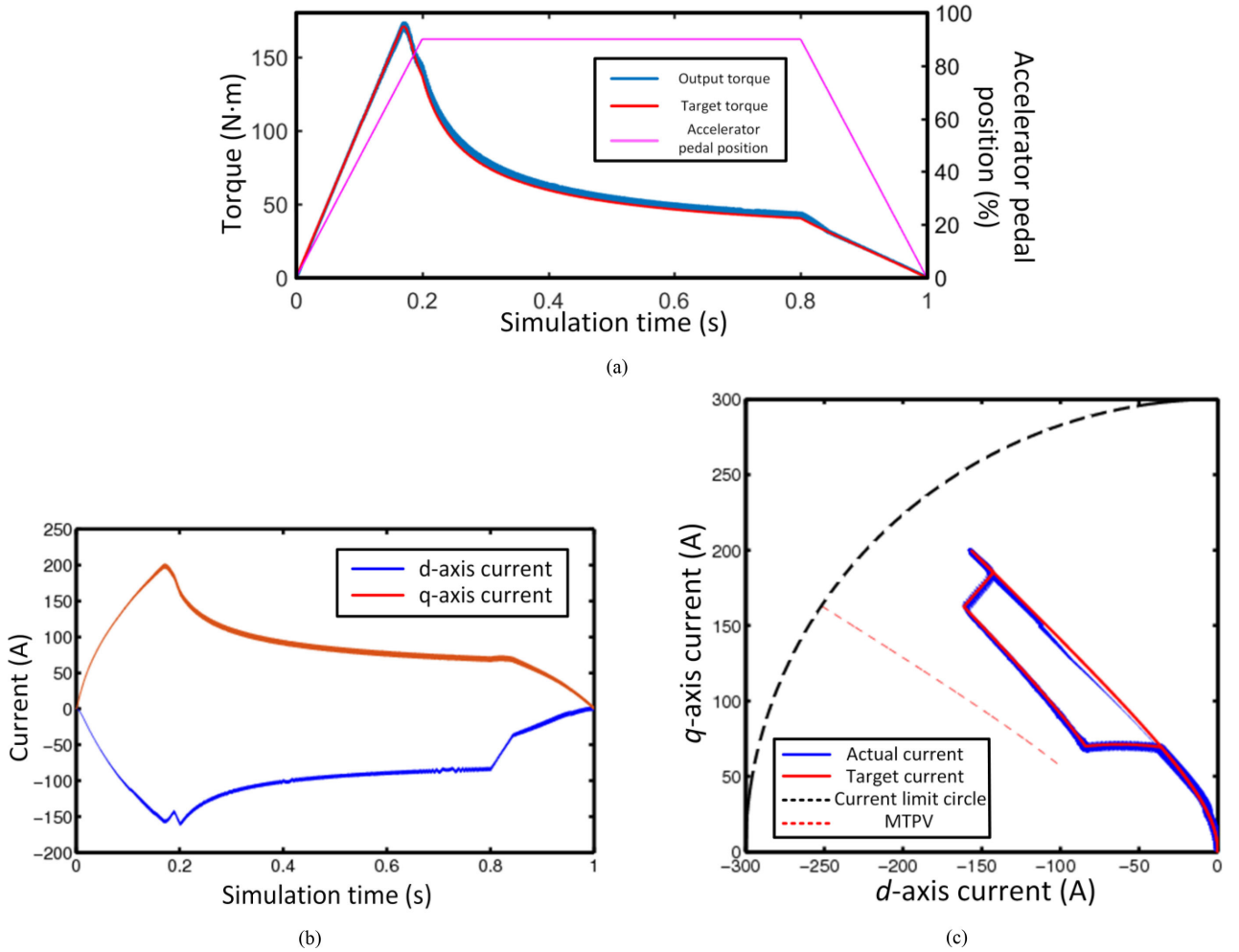

Fig. 13. When $\eta = 1$ in practice. (a) Accelerator pedal position input, output and target torque. (b) *dq*-axes current simulation results. (c) Operation point distribution in the *dq* reference frame.

TABLE II
PERFORMANCE COMPARISON RESULTS

	Method A	Method B	Method C
Mean value of the stator current amplitude (A)	136.162	137.150	133.087
RMS value of the stator current amplitude (A)	141.988	144.953	136.925
Average voltage utilization rate	87.4%	86.0%	88.6%
Average relative error of the output torque	3.42%	4.46%	1.20%

curve and the MTPA trajectory). However, all the analyses above are based on rated parameters of the motor, using which can only provide mediocre results, i.e., a rough approximation of the real behavior. Therefore, an approach is presented in this section to improve the model consistency based on known operation points. The model does not need to describe the motor globally but can capture the local machine behavior considering parameter variations.

The parameters can be settled with respect to the rated current $i_r = [i_{dr}, i_{qr}]^{\mathrm{T}}$ and the rated flux $\lambda_r = [\lambda_{dr}, \lambda_{qr}]^{\mathrm{T}}$ producing the torque T_e using the following equations:

1) the torque equation $3/2(\psi + (L_{\mathrm{d}} - L_q)i_{dr})i_{qr} - T_{\mathrm{e}}/n_{\mathrm{p}} = 0$;
2) the MTPA trajectory $\psi i_d + (L_{\mathrm{d}} - L_q)(i_{dr}^2 - i_{qr}^2) = 0$;
3) the rated current-flux relation $Li_r + \psi_{dq} = \lambda_r$.

where

$$L = \begin{bmatrix} L_d & 0 \\ 0 & L_q \end{bmatrix}, \psi_{dq} = \begin{bmatrix} \psi \\ 0 \end{bmatrix}.$$

For high-speed behavior of an IPMSM, the location of the MTPV trajectory needs to be settled. This can be achieved using the demagnetization current $i_c = [i_{dc}, 0]^{\mathrm{T}}$ that yields the short-circuit current-flux relation $Li_c + \psi_{dq} = 0$.

In addition, the flux-dependent inductances are susceptible to thermal variations according to

$$\psi = \psi_{25^\circ C}(1 - \alpha_\psi \Delta T) \tag{22}$$

where $\psi_{25^\circ C}$ is the PM flux linkage at the room temperature of 25 °C, $\alpha_\psi$is a reversible temperature coefficient (0.0002 Wb/°C

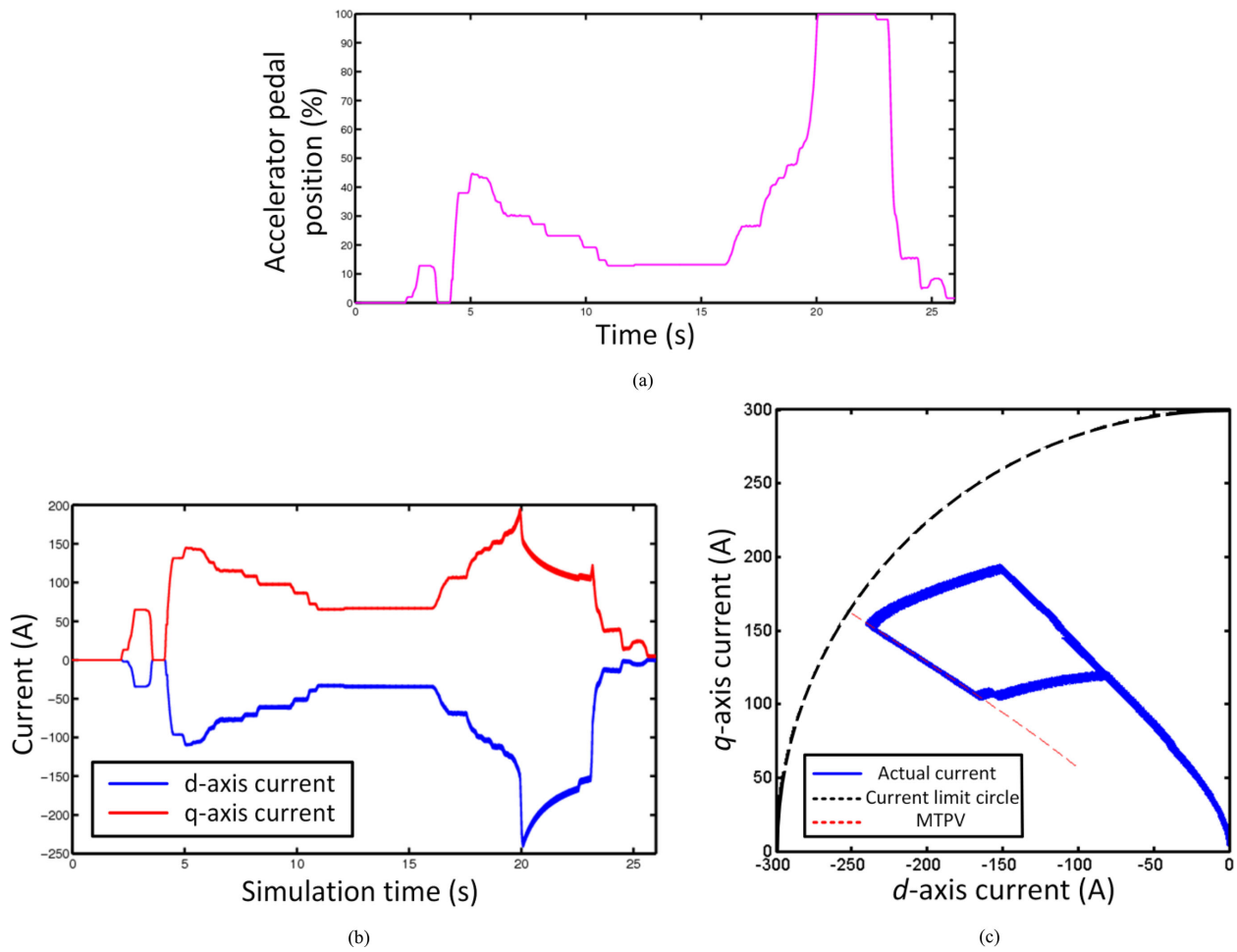

Fig. 14. When η is captured from an electric bus in practice. (a) Accelerator pedal position input. (b) *dq*-axes current experimental results. (c) Operation point distribution in the *dq* reference frame.

for the motor in the article), and $\Delta T{=}T{-}25$ °C. Combining the equations above, the following overdetermined equation system can be achieved for an IPMSM:

$$\begin{bmatrix} \frac{3}{2}i_{dr}i_{qr} & -\frac{3}{2}i_{dr}i_{qr} & -T_e \\ i_{dr}^2 - i_{qr}^2 & i_{qr}^2 - i_{dr}^2 & \\ i_{dr} & & \\ & i_{qr} & \\ i_{dc} & & \end{bmatrix} \begin{bmatrix} L_d \\ L_q \\ 1/n_p \end{bmatrix} = \begin{bmatrix} -1.5\psi i_{qr} \\ -\psi i_d \\ \lambda_{dr} - \psi \\ \lambda_{qr} \\ -\psi \end{bmatrix}. \tag{23}$$

The system (23) can be written compactly as $M\rho = K$ with the least-squares solution $\rho = M^{\dagger}K$, which tends to take account of the temperature effects and generate the machine parameters considering parameter variations. Based on all the concepts introduced above, the procedure to achieve optimal operation can be described by the flowchart in Fig. 10.

VII. Simulation and Experimental Results

In this section, to validate the performance of the proposed optimal FW control approach, simulation and experimental systems were built. Simulations were established in MATLAB/Simulink and the experimental platform was constructed by DSP TMS320F28335 with the sampling frequency of 10 kHz. For the experiment, a three-phase two-level IGBT voltage source converter with a dc bus voltage of 580 V, adopting SVPWM+PI control, was applied. In addition, a dynamometer was used for generating load torque in the motor shaft. The main PMSM parameters used in the simulation and experiment are listed in Table I.

Fig. 11 depicts the simulation results of the optimal operation strategy proposed in Section III with $\eta = 1$ (full throttle) and a 20 N·m constant load torque. $\eta = 1$ indicates that the expected output torque $T_{\rm e}$ equals the maximum torque $T_{\max}$. In other words, the maximum torque curve can be obtained by setting $\eta = 1$. From Fig. 11, it can be seen that the proposed strategy with a PI current controller has the same capability of extending the speed range and tracking the target torque, compared to the conventional speed control. Fig. 11 also presents the switching torque curve, by which the operation area is divided into two zones: Zone I and Zone II. The operation points located in Zone I/II are Type I/II, respectively. Fig. 12 shows the operation point distribution in the *dq* reference frame with $\eta = 1$. At low speed, the operation point lies just on the intersection of the current limit circle and the MTPA trajectory. As the speed increases beyond

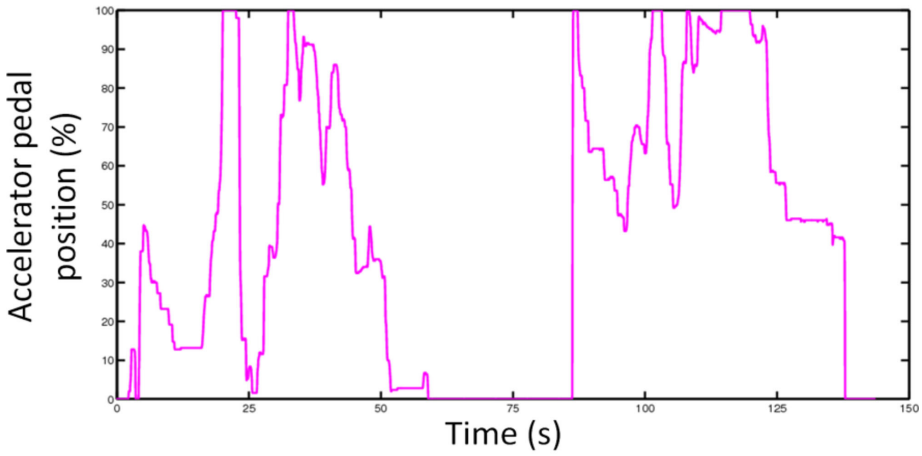

(a)

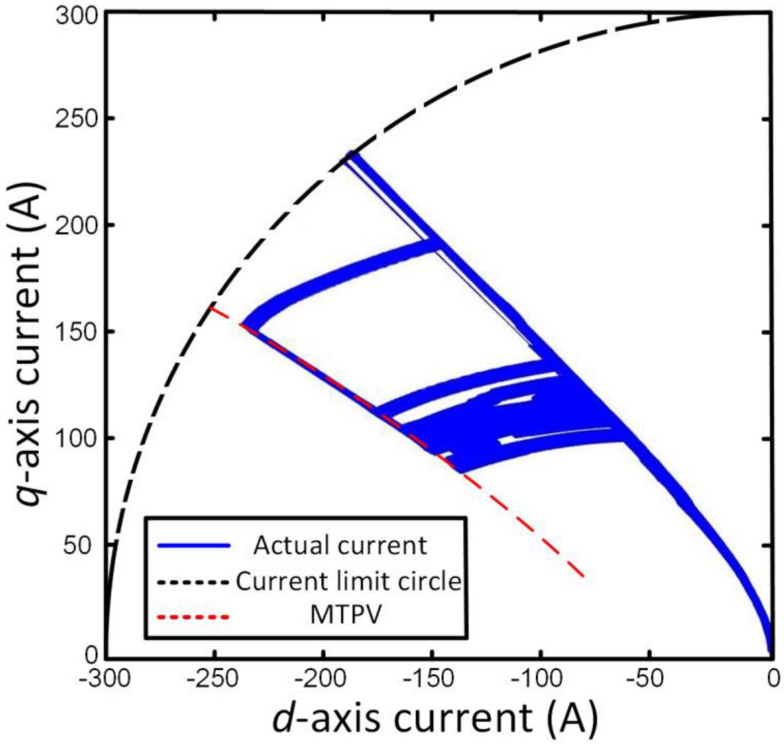

(b)

Fig. 15. When η is captured from CCBC cycle in practice. (a) Accelerator pedal position input. (b) Operation point distribution in the dq reference frame.

the rated operation speed, the intersection is no longer available due to the voltage limit. Thus, the current vector tracks along the current limit circle and then the MTPV trajectory until the output torque and the load torque reach an equilibrium. Considering that every load torque is equivalent to a final output speed, PMSM speed control can be regarded as a particular case ($\eta = 1$) of the torque control, whose target is to reach the reference speed as fast as possible using the maximum available torque.

The accelerator pedal position of $\eta = 1$ in reality is illustrated in Fig. 13(a), which is the slope processing result of the VCU with a safety factor of 0.95. The simulation results of the output torque and the dq-axes current are presented in Fig. 13(a) and (b), respectively. In Fig. 13(c), it is obvious that not only on the characteristic trajectories, but also in the "distribution area" defined in Fig. 1 lie the operation points. Compared to Fig. 12, Fig. 13(c) indicates the main difference between the speed control and the torque control.

It is noteworthy that although the maximum torque curve and the switching torque curve can be obtained by setting $\eta = 1$ in simulations, the premise is that the PMSM model is basically well known. In addition, the curves obtained by simulations usually take no account of the parameter disturbances, making them just nominal ones. To test the parameter independent strategy proposed in Section V, experiments were carried out

on the test bench. Before implementing experimentally, the maximum torque curve and the MTPA curve are calibrated. From Section III, it is known that the switching point must lie on the MTPA trajectory. Therefore, the switching torque curve can be directly obtained from the calibration results. Then, with only one additional operation point calibrated under certain speed, C_0, C_1, C_2 at this speed can be resolved.

Fig. 14(a) illustrates real accelerator pedal position signals captured from an electric bus. In the experiment for the strategy of Section V, equivalent load torques are applied with real position signals as inputs. Fig. 14(b) presents the experimental results of the *dq*-axes current and Fig. 14(c) shows the distribution of the optimal operation points. There, most operation points lie on the MTPA trajectory because the position pedal position η seldom reaches 100%.

Fig. 15(a) shows another real accelerator pedal position signal that is captured from a China city bus typical cycle (CCBC) routine. Differently with Fig. 14(c), it can be seen that in Fig. 15(b) most operation points lie in the zone defined in Fig. 1, which indicates that the operation conditions for the motor are severer than that of Fig. 14(a).

Finally, three methods are compared to indicate the superiority of the proposed strategy assuming the following.

1) *Method A*: Conventional look-up table method.
2) *Method B*: The maximum torque curve and the switching torque curve are calibrated on the test bench. The reference current of the operation point Type II is calculated by (14).
3) *Method C*: The maximum torque curve and the switching torque curve are calibrated on the test bench. The reference current of the operation point Type II is calculated by (19), where C_0 is obtained from the recommended function (21).

Then, with the pedal position input given in Fig. 13(a), the experimental comparison results of the control precision are listed in Table II. There, it can be shown that the proposed strategy is not only more time-saving but also has better performance in output torque precision.

VIII. Conclusion

The presented research in this article proposed a parameter independent approach for EV IPMSMs to obtain the optimal reference current from a given reference torque value at any machine speed. Two characteristic curves, the maximum torque curve and the switching torque curve, are introduced, both of which can be calibrated on a test bench. With the two characteristic torques identified, the optimal operation points over full speed range are classified into two types: Type I and Type II. For Type I, the reference current can be obtained directly from the calibration results. For Type II, to avoid solving complex equations online, a recommended function based on polynomial fitting is proposed. Based on all the aforementioned concepts, the procedure to obtain the reference current becomes completely parameter independent. Compared to the conventional look-up table method, the proposed method is not only more time-saving but also has better performance in the torque output. In further work, high performance current controllers, especially MPC controller, will be combined with the proposed procedure for greater output performance and dynamic response.

Appendix

As analyzed in Section IV, the maximum torque is divided into three modes by the operation speed *n*.

In the constant torque mode, the *dq*-axes current of Point A can be gotten by substituting (7) into (5)

$$\begin{cases} i_{dA} = \dfrac{\psi_f - \sqrt{\psi_f^2 + 8\beta^2 L_d^2 I_{\lim}^2}}{4\beta L_d} \\ i_{qA} = \sqrt{I_{\lim}^2 - i_{dA}^2}. \end{cases} \tag{24}$$

By substituting (24) into (6), $n_A$can be given by

$$n_A = \frac{30U_{\lim}}{\pi n_p \sqrt{L_q^2 I_{\lim}^2 + \psi_f^2 - \frac{C^2(1+\rho)+8C\psi_f}{16\beta}}} \mathrm{r/min} \tag{25}$$

where $C = -\psi_f + \sqrt{\psi_f^2 + 8\beta^2 L_d^2 I_{\lim}^2}$. It shows that the rated operation speed of a PMSM is actually already determined by its own characteristics. However, considering the use safety in practice, the nominal speed of a PMSM on the nameplate is literally a bit lower than its potential rated speed.

In addition, the constant torque T_A can be expressed as following by substituting (24) into (2):

$$T_A = \frac{3\rho(C+4\psi_f)}{32\beta L_d}\sqrt{C^2 + 4C\psi_f}. \tag{26}$$

In the constant power mode, the *dq*-axes current is given by

$$\begin{cases} i_d(n) = \dfrac{-\psi_f + \sqrt{\psi_f^2 + (\rho^2-1)\left(\psi_f^2 + \rho^2 L_d^2 I_{\lim}^2 - \dfrac{900U_{\lim}^2}{\pi^2 n_p^2 n^2}\right)}}{L_d(1-\rho^2)} \\ i_q(n) = \sqrt{I_{\lim}^2 - i_d^2(n)}. \end{cases} \tag{27}$$

Then, $T_{\max}$ of the constant power mode can be obtained by substituting (27) into (2).

Similarly, the *dq*-axes current of the decreased power mode can be computed by combining (6) and (8). Then, $T_{\max}$ can be easily resolved by substituting the current result into (2).

References

[1] Y. Zhang, D. Xu, J. Liu, S. Gao, and W. Xu, "Performance improvement of model-predictive current control of permanent magnet synchronous motor drives," *IEEE Trans. Ind. Appl.*, vol. 53, no. 4, pp. 3683–3695, Jul./Aug. 2017.

[2] Z. Mynar, L. Vesely, and P. Vaclavek, "PMSM model predictive control with field-weakening implementation," *IEEE Trans. Ind. Electron.*, vol. 63, no. 8, pp. 5156–5166, Aug. 2016.

[3] D. Casadei, F. Profumo, G. Serra, and A. Tani, "FOC and DTC: Two viable schemes for induction motors torque control," *IEEE Trans. Power Electron.*, vol. 17, no. 5, pp. 779–787, Sep. 2002.

[4] L. Zhong, M. Rahman, W. Hu, and K. Lim, "Analysis of direct torque control in permanent magnet synchronous motor drives," *IEEE Trans. Power Electron.*, vol. 12, no. 3, pp. 528–536, May 1997.

[5] Z. Zhang, R. Ma, L. Wang, and J. Zhang, "Novel PMSM control for anti-lock braking considering transmission properties of the electric vehicle," *IEEE Trans. Veh. Technol.*, vol. 67, no. 11, pp. 10378–10386, Nov. 2018.

[6] N. Bianchi and S. Bolognani, "Parameters and volt-ampere ratings of a synchronous motor drive for flux-weakening applications," *IEEE Trans.Power Electron.*, vol. 12, no. 5, pp. 895–903, Sep. 1997.

[7] K. Kamiev, J. Montonen, M. Ragavendra, J. Pyrhonen, J. Tapia, and M. Niemela, "Design principles of permanent magnet synchronous machines for parallel hybrid or traction applications," *IEEE Trans. Ind. Electron.*, vol. 60, no. 11, pp. 4881–4890, Nov. 2013.

[8] M. Preindl and S. Bolognani, "Optimal state reference computation with constrained MTPA criterion for PM motor drives," *IEEE Trans. Power Electron.*, vol. 30, no. 8, pp. 4524–4535, Aug. 2015.

[9] M. Preindl and S. Bolognani, "Model predictive direct torque control with finite control set for PMSM drive systems, part 1: Maximum torque per ampere operation," *IEEE Trans. Ind. Inform.*, vol. 9, no. 2, pp. 1912–1921, Nov. 2013.

[10] S.-Y. Jung, J. Hong, and K. Nam, "Current minimizing torque control of the IPMSM using Ferrari's method," *IEEE Trans. Power Electron.*, vol. 28, no. 12, pp. 5603–5617, Dec. 2013.

[11] S. Zhao, Y. Chen, and Y. Mao, "Adaptive load observer-based feed-forward control in PMSM drive system," *Trans. Inst. Meas. Control*, vol. 37, no. 3, pp. 414–424, 2015.

[12] T. Tarczewski and L. M. Grzesiak, "Constrained state feedback speed control of PMSM based on model predictive approach," *IEEE Trans. Ind. Electron.*, vol. 63, no. 6, pp. 3867–3875, Jun. 2016.

[13] C. Xia, N. Liu, Z. Zhou, Y. Yan, and T. Shi, "Steady-state performance improvement for LQR-based PMSM drives," *IEEE Trans. Power Electron.*, vol. 33, no. 12, pp. 10622–10632, Dec. 2018.

[14] S. Gao, H. Dong, B. Ning, T. Tang, and Y. Li, "Nonlinear mapping-based feedback technique of dynamic surface control for the chaotic PMSM using neural approximation and parameter identification," *IET Control Theory Appl.*, vol. 12, no. 6, pp. 819–827, 2018.

[15] L. Wang and D.-N. Truong, "Stability enhancement of a power system with a PMSG-based and a DFIG-based offshore wind farm using a SVC with an adaptive-network-based fuzzy inference system," *IEEE Trans. Ind. Electron.*, vol. 60, no. 7, pp. 2799–2807, Jul. 2013.

[16] J. Choi, K. Nam, A. A. Bobtsov, A. Pyrkin, and R. Ortega, "Robust adaptive sensorless control for permanent-magnet synchronous motors," *IEEE Trans. Power Electron.*, vol. 32, no. 5, pp. 3989–3997, May 2017.

[17] M. Preindl, E. Schaltz, and P. Thøgersen, "Switching frequency reduction using model predictive direct current control for high-power voltage source inverters," *IEEE Trans. Ind. Electron.*, vol. 58, no. 7, pp. 2826–2835, Jul. 2011.

[18] Y. Feng, X. Yu, and F. Han, "High-order terminal sliding-mode observer for parameter estimation of a permanent-magnet synchronous motor," *IEEE Trans. Ind. Electron.*, vol. 60, no. 10, pp. 4272–4280, Oct. 2013.

[19] X. Liu, H. Chen, J. Zhao, and A. Belahcen, "Research on the performances and parameters of interior PMSM used for electric vehicles," *IEEE Trans. Ind. Electron.*, vol. 63, no. 6, pp. 3533–3545, Jun. 2016.

[20] A. H. Abosh, Z. Q. Zhu, and Y. Ren, "Reduction of torque and flux ripples in space vector modulation-based direct torque control of asymmetric permanent magnet synchronous machine," *IEEE Trans. Power Electron.*, vol. 32, no. 4, pp. 2976–2986, Apr. 2017.

[21] M. Preindl and E. Schaltz, "Sensorless model predictive direct current control using novel second-order PLL observer for PMSM drive systems," *IEEE Trans. Ind. Electron.*, vol. 58, no. 9, pp. 4087–4095, Aug. 2011.

[22] Y. Inoue, S. Morimoto, and M. Sanada, "Comparative study of PMSM drive systems based on current control and direct torque control in flux-weakening control region," *IEEE Trans. Ind. Appl.*, vol. 48, no. 6, pp. 2382–2389, Nov./Dec. 2012.

[23] T. Miyajima, H. Fujimoto, and M. Fujitsuna, "A precise model-based design of voltage phase controller for IPMSM," *IEEE Trans. Power Electron.*, vol. 28, no. 12, pp. 5655–5664, Dec. 2013.

[24] M. Siami, D. A. Khaburi, M. Rivera, and J. Rodríguez, "A computationally efficient lookup table based FCS-MPC for PMSM drives fed by matrix converters," *IEEE Trans. Ind. Electron.*, vol. 64, no. 10, pp. 7645–7654, Oct. 2017.

[25] B. Cheng and T. R. Tesch, "Torque feedforward control technique for permanent-magnet synchronous motors," *IEEE Trans. Ind. Electron.*, vol. 57, no. 3, pp. 969–974, Mar. 2010.

[26] R. H. Park, "Two-reaction theory of synchronous machines generalized method of analysis—Part I," *Trans. Amer. Inst. Elect. Eng.*, vol. 48, pp. 716–727, 1929.

[27] S. Boyd and L. Vandenberghe, in *Convex Optimization*. Cambridge, U.K.: Cambridge Univ. Press, 2004. [Online]. Available: http://www.stanford.edu/boyd/cvxbook/

[28] M. Zordan, P. Vas, M. Rashed, S. Bolognani, and M. Zigliotto, "Field-weakening in high-performance PMSM drives: A comparative analysis," in *Proc. Ind. Appl. Conf.*, 2000, pp. 1718–1724.

[29] S. Bolognani, S. Calligaro, R. Petrella, and F. Pogni, "Flux-weakening in IPM motor drives: Comparison of state-of-art algorithms and a novel proposal for controller design," in *Proc. Eur. Conf. Power Electron. Appl.*, 2011, pp. 1–11.

[30] W. Wang and X. Xi, "Current control method for PMSM with high dynamic performance," in *Proc. IEEE Int. Elect. Mach. Drives Conf.*, 2013, pp. 1249–1254.

[31] A. Ahmed, Y. Sozer, and M. Hamdan, "Maximum torque per ampere control for buried magnet PMSM based on DC-link power measurement," *IEEE Trans. Power Electron.*, vol. 32, no. 2, pp. 1299–1311, Feb. 2017.

[32] J. Lemmens, P. Vanassche, and J. Driesen, "PMSM drive current and voltage limiting as a constraint optimal control problem," *IEEE J. Emerg. Sel. Topics Power Electron.*, vol. 3, no. 2, pp. 326–338, Jun. 2015.